

# Future Change in Extratropical Cyclones Associated with Change in the Upper Troposphere

RYO MIZUTA

*Meteorological Research Institute, Tsukuba, Japan*

MIO MATSUEDA

*Japan Agency for Marine-Earth Science and Technology, Tsukuba, Japan*

HIROKAZU ENDO AND SEIJI YUKIMOTO

*Meteorological Research Institute, Tsukuba, Japan*

(Manuscript received 2 August 2010, in final form 31 March 2011)

## ABSTRACT

Future changes in Northern Hemisphere wintertime storm activity as a consequence of global warming are investigated using the AGCM of Meteorological Research Institute (MRI-AGCM) with horizontal grid sizes of 60 and 20 km. A future (2075–99) climate experiment, in which the change in sea surface temperature (SST) derived from the Coupled Model Intercomparison Project phase 3 (CMIP3) multimodel ensemble mean is added to observed SST, is compared with a present-day (1979–2003) climate experiment. Results of three-member simulations using the 60-km model are presented. A single simulation using the 20-km model is also presented, showing that similar results are obtained.

In the future climate experiment, the number of intense cyclones (sea level pressure below 980 hPa) shows a significant increase whereas the number of total cyclones shows a significant decrease, similar to the results obtained from the CMIP3 models themselves. The increase in intense cyclones is seen on the polar side and downstream side of Atlantic and Pacific storm tracks. At the same time, the growth rate of the cyclones increases in areas upstream of these regions.

For the regions with the increasing growth rate, a high correlation is seen between the growth rate of the surface cyclones and upper-tropospheric zonal wind at a monthly-mean time scale. Months of high cyclone growth rate with strong zonal wind in these regions become more frequent, and months of low cyclone growth rate with weak zonal wind become less frequent. One of the possibilities that can explain this relationship is changes in the wave-breaking pattern, that is, a decrease in wave breakings in areas of cyclonic shear and an increase in wave breakings in areas of anticyclonic shear. Associated with these changes, rapid cyclone developments are more commonly seen, and weak, long-lived cyclones become less frequent.

## 1. Introduction

The activity of extratropical cyclones is a dominant weather feature in the midlatitudes during the period from autumn to spring. Any change in this activity due to global warming would have a marked influence on the daily lives of many people. In particular, a change in the occurrence of intense cyclones could influence the scale and frequency of disasters resulting from extreme wind

or precipitation events. The changes in cyclone activity likely to occur with a warmer climate remain insufficiently understood, especially with regard to extreme cyclones (Solomon et al. 2007).

According to the results of climate models that contributed to the Coupled Model Intercomparison Project phase 3 (CMIP3; Meehl et al. 2007), synoptic-scale activity (so-called storm-track activity) increases in the middle–upper troposphere in future climate experiments compared with present-day experiments. Yin (2005) reported that the zonal-mean eddy kinetic energy at a synoptic time scale shows an increase in future climate experiments, and that its peak shifts poleward and

---

*Corresponding author address:* Ryo Mizuta, Meteorological Research Institute, 1-1 Nagamine, Tsukuba 305-0052, Japan.  
E-mail: rmizuta@mri-jma.go.jp

slightly to the higher level. This change is consistent with the temperature change expected in the middle–upper troposphere around 200–500 hPa. Whereas greater warming occurs in the tropics because of increased vertical water vapor flux and latent heat release, relatively little warming occurs at high latitudes. This occurs because the tropopause is located lower at high latitudes than in the tropics, so high-latitude regions at these levels are more affected by the air of the stratosphere, where the temperature is decreasing because of increased radiative cooling by CO<sub>2</sub>. Therefore, the meridional temperature gradient at these levels is intensified in the future, resulting in stronger synoptic-scale activity in response to the meridional temperature gradient. While the increase in synoptic-scale activity is larger in the upper levels, the increase is also seen in the middle troposphere (Pinto et al. 2007) and near the surface (Ulbrich et al. 2008), although the signal near the surface is relatively weak and limited to specific regions that depend on the model.

According to the same set of results of climate models, the total number of surface cyclone tracks decreases in the future experiments (Lambert and Fyfe 2006). Such a decrease has been reported in many studies (Geng and Sugi 2003; Bengtsson et al. 2006), as reviewed by Ulbrich et al. (2009). This change is consistent with the temperature change expected in the lower troposphere that warming is greater at high latitudes than in the tropics. The most well-known explanation of larger warming at high latitudes is that the melting of snow cover and sea ice induces a change in surface albedo, leading in turn to more warming (e.g., Hall 2004), although Winton (2006) argues that other radiative feedbacks also contribute to it. Consequently, the meridional temperature gradient near the surface becomes weaker than the present gradient, resulting in weaker baroclinicity in the lower troposphere. The reduced baroclinicity is often explained as the cause of decrease in cyclone number.

Apparently, the decrease in the number of cyclones and the increase in the synoptic-scale activity do not seem to be consistent with each other. Another change that many of the models predict is an increasing number of intense cyclones. Lambert and Fyfe (2006) showed that the frequency of extreme cyclones (sea level pressure below 970 hPa) in winter is expected to increase in the future experiments in a large part of the CMIP3 models. The increase in intense cyclones is limited to some areas, depending on models and experiments. Regions near the British Isles and Aleutian Islands show an increase in some models (Geng and Sugi 2003; Pinto et al. 2007). These regions are corresponding to those of increasing storm-track activity near the surface in the ensemble mean of CMIP3 experiments (Ulbrich et al. 2008). While the increase in the number of intense

cyclones could explain the increase in the synoptic-scale activity, the reason for this increase in intense cyclones remains unclear, although some studies suggested the increase is related to the enhanced latent heat release (e.g., Geng and Sugi 2003).

Extratropical cyclones are categorized into the following two types based on their life cycles (LCs) of LC1 and LC2 (Thorncroft et al. 1993; Shapiro et al. 1999). The former corresponds to cyclones that develop within anticyclonic shear, accompanied by anticyclonic Rossby wave breakings, whereas the latter corresponds to cyclonic shear and cyclonic breakings. Idealized numerical experiments show that these two types of extratropical cyclones have different developments (Wernli et al. 1998). Averaged cyclone developments are more rapid under anticyclonic wave breakings, and lifetimes of the cyclones become longer under cyclonic wave breakings due to suppressed energy conversion (Thorncroft et al. 1993; Watanabe 2009). In the real atmosphere, rapid cyclone development is triggered by upper-tropospheric Rossby waves (Yoshiike and Kawamura 2009). The results of the above studies suggest that future change in the upper troposphere associated with global warming may influence the development of extratropical cyclones.

The present study investigates how the global warming–related changes in the middle–upper troposphere and those near the surface are explained consistently; that is, the relationships between enhanced storm-track activity, reduced number of total cyclones, and increased number of intense cyclones under the opposed change in meridional temperature gradient between the upper troposphere and near the surface. We focus on regional changes in upper-tropospheric background flows and in growth rates of surface cyclones. Roles of cyclonic/anticyclonic patterns of wave breakings are also considered.

Changes during the Northern Hemisphere winter are studied by comparing the present-day climate and the future climate in a high-resolution atmospheric general circulation model (AGCM) that can simulate the structures of intense cyclones. By using the change in sea surface temperature (SST) and sea ice concentration from the CMIP3 multimodel ensemble as the lower-boundary conditions in the model, we obtained high-resolution data on atmospheric change similar to that predicted by a multimodel ensemble. Because the climate of extratropical winter shows large interannual variability, three members of 25-yr simulations with initial-value ensemble approach are analyzed to extract statistically significant changes.

The remainder of this paper is organized as follows. The model and the method of cyclone detection are described in section 2. Section 3 presents the results regarding future changes in cyclone behavior, background

flows, and the relations between these factors. Finally, section 4 contains the discussion and conclusions.

## 2. Model and methodology

### a. Model outline

This study uses Meteorological Research Institute Atmospheric General Circulation Model version 3.1, (MRI-AGCM3.1), a global atmospheric general circulation model jointly developed by the Japan Meteorological Agency and the MRI. Details of the model can be found in Mizuta et al. (2006), who showed that the global distributions of the seasonal-mean atmospheric fields, precipitation, and surface air temperature simulated by the 20-km-mesh version of the model agree well with observations. Moreover, the model yields improved representation of regional-scale phenomena and local climate as a result of increased horizontal resolution, thereby yielding an improved expression of topographical effects and physical processes without degrading the representation of global climate.

Here, we use the results of present-day and future climate experiments performed using the above model (Kitoh et al. 2009). For the present-day climate experiment, from 1979 to 2003, monthly-mean observed SST and sea ice concentration by the Hadley Center (Rayner et al. 2003) are given as the lower-boundary conditions. For the future climate experiment, from 2075 to 2099, the SST is prepared by superposing (i) the detrended observed SST, including year-to-year variability; (ii) future change in the multimodel ensemble mean (MEM) of SST; and (iii) the linear trend in the MEM of SST projected by CMIP3 models. Future change in the MEM of SST was evaluated by the difference between twentieth-century simulations and future simulations conducted under the Special Report on Emission Scenario (SRES) A1B emission scenario. The design retains observed year-to-year variability, such as El Niño–Southern Oscillation (ENSO) events, in the future climate. Future sea ice distribution is obtained in a similar fashion. Details of the method can be found in Mizuta et al. (2008). The concentrations of greenhouse gases are also changed following the A1B emission scenario.

We use the simulations performed with horizontal resolutions of 60 and 20 km. The 60-km model has  $640 \times 320$  grid cells, corresponding to a triangular truncation of 319 with a linear Gaussian grid (TL319) in the horizontal. The 20-km model has  $1920 \times 960$  grid cells with TL959. Both models have 60 layers in the vertical, with the model top at 0.1 hPa. In addition, for comparison with the Japanese 25-year Reanalysis (JRA-25; Onogi et al. 2007), the results of a 120-km model (TL159, 40 layers) are presented because the reanalysis was made

using a horizontal resolution of 120 km. The model settings are the same among the three resolutions, except for several tuning parameters that are altered to reduce the resolution dependence of the results.

Although the higher-resolution model is more realistic in representing phenomena such as blockings (Matsueda et al. 2009), the length of the simulation is limited by computational resources. We performed three pairs of the present and future experiments with the 60-km model, which use the same boundary conditions but start from different initial values, while only a single pair of the experiments is obtained with the 20-km model. Consequently, we focus on the results of the 60-km simulations to obtain the nature of changes between the present and future climates. The 20-km results are also presented to show the robustness of this approach, in that similar results are obtained for a higher-resolution model.

### b. Method of cyclone tracking

The method of cyclone detecting and tracking employed in the present study is a modified version of that described by Geng and Sugi (2003). The method uses 6-hourly sea level pressure (SLP) interpolated to a  $1.25^\circ$  grid. As the detecting step, points with SLP lower than the surrounding 8 points and with SLP more than 0.3 hPa lower than the average of the surrounding 8 points are identified as cyclones. Points at elevations higher than 1500 m above sea level are excluded from analysis. Next, as the tracking step, each point is advected by the background flow (15-day running mean of 700-hPa wind), and search the nearest point within 300 km at the next time step. We use 700-hPa wind as a representation of the lower troposphere from surface to about 500 hPa, and use a 15-day running mean to remove the fluctuation by the cyclone itself. If the point is found, the two related points are regarded as one sequence of a cyclone. This method is relatively simple compared with those proposed in recent studies [see the review by Ulbrich et al. (2009)] and has arbitrary parameters, especially in the tracking step. However, the results shown here are largely independent of the details of the method, as we focus on the difference between the two experiments and on the pressure change between successive steps during the developing stage of cyclones.

Figures 1a–d show cyclone tracks from December to February (DJF) for two winters (2000/01 and 2001/02), as derived from JRA-25 and the 120-, 60-, and 20-km models. Cyclones that persist for longer than 24 h and experience below 1010 hPa are shown. Cyclone tracks in the Pacific (from Korea and Japan to Alaska and the west coast of North America) and in the Atlantic (from central North America to the Norwegian Sea and northern coast of Russia) are well simulated at all resolutions. Cyclone

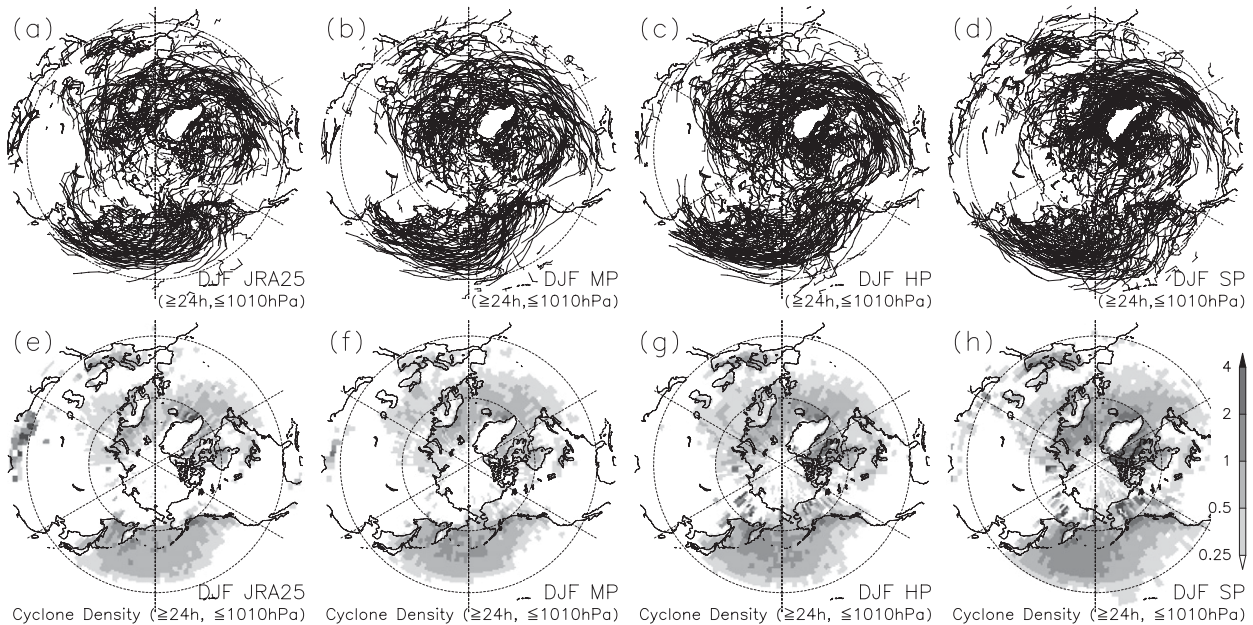


FIG. 1. (a)–(d) Cyclone tracks from DJF for two winters (2000/01 and 2001/02), and (e)–(h) the cyclone density within  $2.5^\circ$  grid boxes (1 per month per box) for DJF over a 25-yr period. Cyclones that persist for longer than 24 h and experience below 1010 hPa are shown, for (a),(e) JRA-25, (b),(f) the 120-km model, (c),(g) the 60-km model, and (d),(h) the 20-km model.

tracks are also seen in the Mediterranean Sea. Difference between the reanalysis data and models is found at low latitudes, around India and the tropical eastern Pacific.

Figures 1e–h show the cyclone density for the 25-yr period (1979 to 2003). The density is defined as the frequency of existence of cyclones that persist for longer than 24 h and experience below 1010 hPa. The density for each  $2.5^\circ$  grid box is shown. The horizontal resolution of the reanalysis is the same as that in the 120-km model, and these two have similar results. The 60- and 20-km models show slightly more tracks than in the 120-km model and reanalysis data. Weak disturbances are captured more frequently in higher-resolution models when using this type of method (Jung et al. 2006), even if all the results are interpolated to a  $1.25^\circ$  grid. However, the spatial distribution of densities during the Northern winter is well simulated at all resolutions. Although tropical cyclones are also captured using this method, as seen in the tracks at low latitudes, we treat all cyclones in the region  $20^\circ$ – $90^\circ$ N as extratropical cyclones because tropical cyclones are rare in this region during winter.

### 3. Results

#### a. Change in cyclone frequency

Here, we examine the change in cyclone tracks from the present-day experiments to the future experiments.

Figure 2 shows the total cyclone track number in the region  $20^\circ$ – $90^\circ$ N during winter as a function of threshold minimum SLP. Cyclones that persist for longer than 24 h and whose minimum SLP during the lifetime is lower than each threshold value are counted. The rates of change from the present-day experiments to the future experiments are plotted in the lower panel, showing the statistical significance of the change (Student's *t* test). When a higher SLP threshold is used to capture almost all the cyclones, the number of cyclones decreases in the future experiments. The decrease is 10%–20% and is statistically significant in both the 60- and 20-km models. However, for an SLP threshold of below 980 hPa, in which case only intense cyclones are detected, the number of cyclones increases by 10%–20%. This change is consistent with the results obtained using CMIP3 models (Lambert and Fyfe 2006) and the results presented by Bengtsson et al. (2009). The increase is statistically significant only in the 60-km model. It is noted that the significance is obtained from averaging of the three experiments, not from the difference in horizontal resolution. If we compare a single member of the present-day experiments with a single member of the future experiments, the increase is not statistically significant.

Figure 3 shows whether the results of Fig. 2 depend on the lifetime threshold of the cyclones. Cyclones that persist for longer than 48, 72, and 96 h in the 60-km model are counted, respectively, while the value of 24 h is used in Fig. 2. The decrease in the number of all

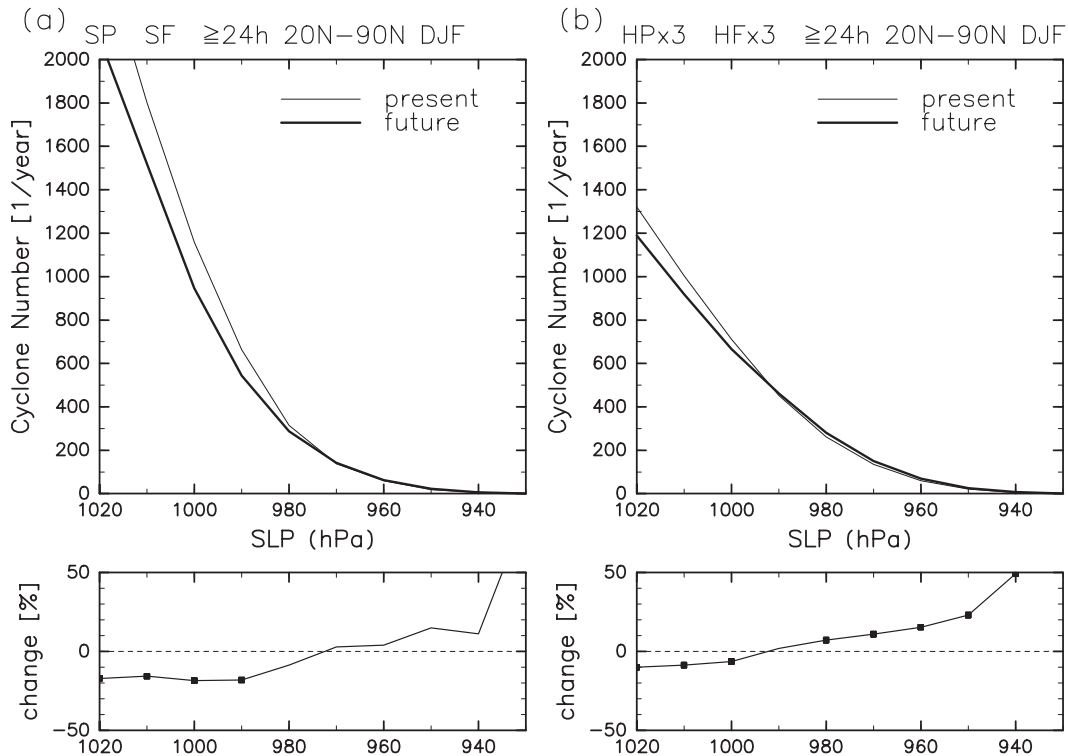


FIG. 2. Number of cyclones in the region  $20^{\circ}$ – $90^{\circ}$ N in DJF as a function of the threshold minimum sea level pressure for (a) the 20-km model and (b) the three-member mean of the 60-km models. Units are  $1 \text{ yr}^{-1}$ . Thin lines indicate the present-day experiments, and thick lines indicate the future experiments. (bottom) The rate of change from the present-day to future experiments is shown. Dots indicate that the change is significant at the 99% level (Student's  $t$  test).

cyclones is more remarkable when the longer lifetime threshold is taken. For an SLP threshold of 1000 hPa, for instance, a decrease of over 30% is seen in the cyclones longer than 96 h, while there is about 10% decrease in those longer than 24 h. The increase in intense cyclones does not depend much on the lifetime. About 20% increase for an SLP threshold of 960 hPa, and about 50% increase for 940 hPa in any lifetime thresholds, although statistical significance is smaller in the region of long lifetime thresholds and lower SLP thresholds due to the smaller sample number.

Figures 4a and 4b show the horizontal distribution of cyclone density for all cyclones ( $\leq 1010$  hPa) and its future change for the 60-km model. A future decrease in cyclone density is seen in large parts of regions where cyclones are frequently seen, including the Pacific and the Atlantic storm tracks. A relatively large decrease is seen in the Mediterranean Sea. An increase is seen only in the northern part of the Sea of Okhotsk, Baffin Bay, and in parts of the Arctic sea. These areas correspond to regions of sea ice retreat and large changes in surface temperature. The cyclone density and its change in intense cyclones ( $\leq 980$  hPa) are shown in Figs. 4c and 4d.

In the areas east of Japan and east of Canada, which are in the first half of storm tracks, intense cyclones decrease as well as weak cyclones. In contrast, an increase in intense cyclones is seen in the latter half of storm tracks, from the east coast of Russia to the west coast of Alaska and Canada and from Scotland to the north coast of Russia. In these areas, an increase is also seen in seasonal precipitation amount and frequency of strong wind (e.g., exceeding  $25 \text{ m s}^{-1}$ ) (not shown).

It is speculated from the above changes that the development of individual cyclones in storm-track regions could change under the future climate. Then we calculated the growth rate of storms, defined as temporal SLP change along each cyclone track. These values were averaged for the cyclones that pass through each of the  $2.5^{\circ}$  grid boxes. Figure 5 shows the distribution of the average growth rate and its future change. The average growth rate in the present-day experiments (Fig. 5a) is largest at about  $40^{\circ}$ N in the Pacific and  $45^{\circ}$ N in the Atlantic. The growth rate increases on the polar side of the peak latitudes but decreases on the equatorial side (Fig. 5b). The contrast between increasing and decreasing trends is more pronounced in the Pacific region than in

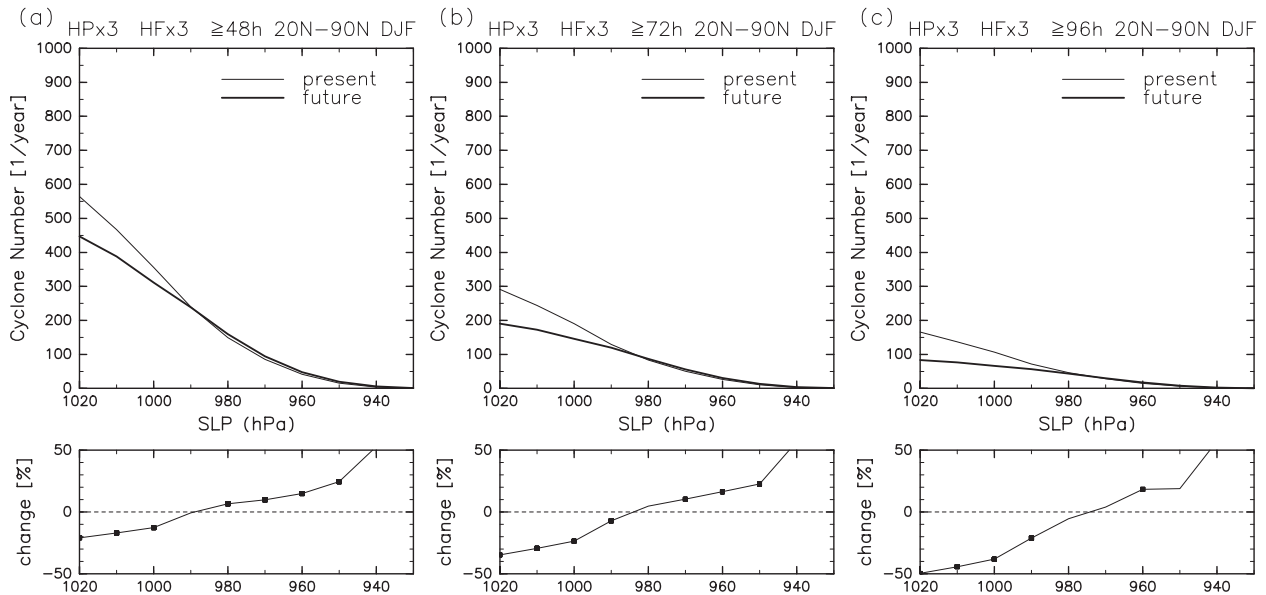


FIG. 3. As in Fig. 2, but for cyclones with lifetimes longer than (a) 24, (b) 48, and (c) 96 h for the three-member mean of the 60-km models.

the Atlantic. In the Atlantic, a large increase in growth rate is seen upstream of the British Isles. The increase in the density of intense cyclones (Fig. 4d) is seen downstream of regions with an increase in growth rate. Therefore, combined with the fact that the increase in intense cyclones does not depend much on the lifetime (Fig. 3), the increased density of intense cyclones can be explained by the increase in growth rate.

#### b. Future changes in background fields

To investigate what part of the changes in the background fields are related to changes in cyclone behavior, we examined changes in the three-dimensional seasonal-mean fields. Figures 6a and 6b show the zonal mean temperature in the present-day experiments and the difference between the present-day and future experiments. The contours show values of the present-day experiments, and shading indicates the difference between the present-day and future experiments. The future change below 850 hPa corresponds to the surface temperature change, which shows a larger increase at high latitudes than at low latitudes. The meridional temperature gradient becomes smaller at these altitudes. In the upper troposphere (150–400 hPa), the temperature increase is large in the tropics but small at high latitudes. Figures 6c and 6d show the future change in the zonal mean eddy kinetic energy at the synoptic time scale (2.5–8.0 days). The region of high activity shifts to higher latitudes and activity increases. The increase is more pronounced in the upper levels, although a small increase is still seen at lower levels. These results are common to the 20-km model and

the 60-km model and similar to those obtained from the multimodel ensemble mean (Yin 2005).

Here, changes in the upper troposphere are compared with those in the lower troposphere. Figure 7 shows the horizontal distribution of future change in zonal wind, eddy kinetic energy, and the maximum Eady growth rate (Lindzen and Farrell 1980) at the upper level (300 hPa) and the lower level (850 hPa). The maximum Eady growth rate  $\sigma$  is as an index of baroclinicity, calculated as  $\sigma = 0.31 gN^{-1}T^{-1}\nabla T$ , where  $T$  is temperature and  $N$  is the Brunt–Väisälä frequency. Daily values of  $\sigma$  are calculated, and they are averaged over DJF. The data are from the 60-km experiments, although similar results were obtained in the 20-km experiments.

Figure 7a shows the horizontal distribution of future change in the zonal wind at 300 hPa. The subtropical jet becomes weaker around northern Africa and south of Japan. The jet extends to downstream areas, showing an increase around the eastern Pacific and from the eastern Atlantic to Europe. The wind is enhanced also from northeastern Asia to north of Japan, indicating that the polar jet becomes stronger. The patterns of change in the western Pacific and eastern Atlantic are similar to those of the cyclone growth rate (Fig. 5b). The extension of the jet indicates the eastward extension of momentum flux convergence in the latter part of the jet. Open and closed circles indicate the locations of maximum wind for each longitude, for the present-day and future experiments, respectively. The shift of the locations of the maximum wind is very small. Thus, in this model, it is more appropriate to say that the jet is broadened with

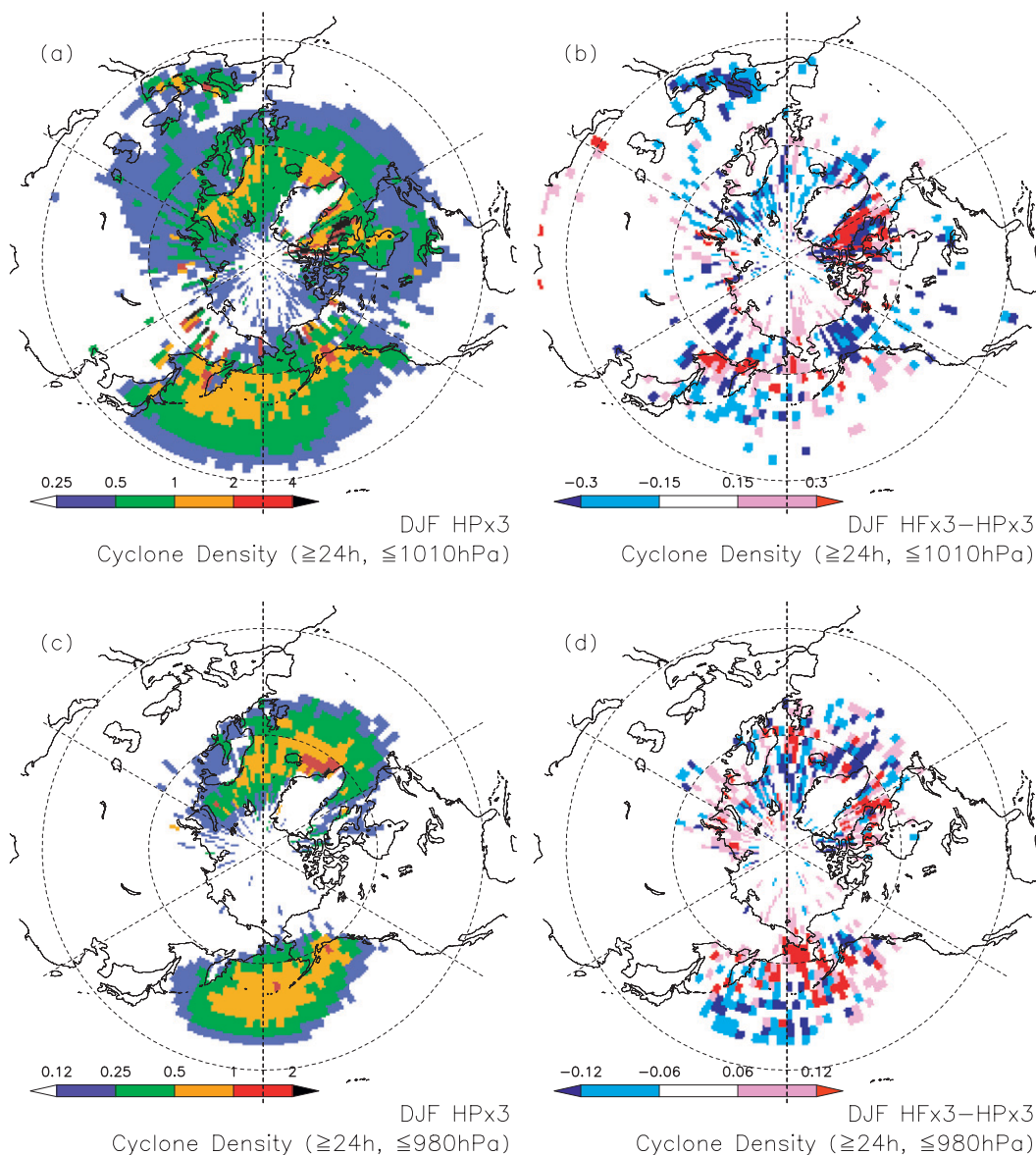


FIG. 4. Horizontal distributions of cyclone density in DJF of (a),(c) the present-day experiments and (b),(d) the change from the present-day to future experiments for (a),(b) all cyclones ( $\leq 1010$  hPa) and (c),(d) intense cyclones ( $\leq 980$  hPa) for the three-member mean of the 60-km models. The density of cyclones that persist for longer than 24 h is calculated for each  $2.5^\circ$  grid box. Units are 1 per month per box.

the enhanced polar jet and the reduced subtropical jet, rather than that the subtropical jet is shifted poleward.

Figure 7b shows the future change in the eddy kinetic energy at a synoptic time scale at 300 hPa. An increase is seen at almost all longitudes of  $40^\circ$ – $50^\circ\text{N}$ , corresponding to the zonal-mean increase in Fig. 6d. Stronger increase is seen from the eastern Atlantic to Europe and from northeastern Asia to north of Japan. These regions are also similar to the regions of an increase in the polar jet (Fig. 7a).

The future change in  $\sigma$  at 300 hPa is shown in Fig. 7c. An increase in  $\sigma$  is seen across large areas of the

extratropics at 300 hPa. The increase is mainly from strengthening of the meridional temperature gradient in midlatitudes, and from the decrease in static stability due to the change in the vertical (potential) temperature gradient. This is speculated from Figs. 6a and 6b, and can be seen by dividing the change in  $\sigma$  into  $\Delta\sigma \sim [\Delta(\nabla T/T)/(\nabla T/T)]\sigma + [\Delta(1/N)/(1/N)]\sigma$  and calculating each component (not shown). Overall, the situation in the upper troposphere is promoting more activity of the synoptic-scale waves, although the change in  $\sigma$  is not so similar to the cyclone growth rate (Fig. 5b) in the

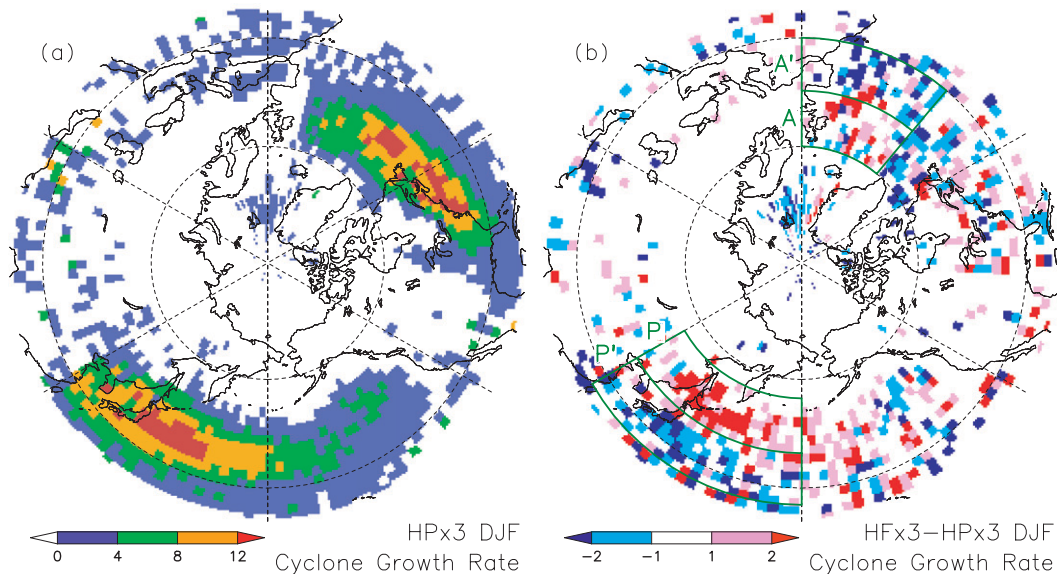


FIG. 5. Horizontal distributions of the mean growth rate of cyclones ( $\text{hPa day}^{-1}$ ) in DJF of (a) the present-day experiments and (b) the change from the present-day to future experiments for the three-member mean of the 60-km models. The areas outlined by green lines are referred to in Fig. 8.

horizontal pattern and does not seem to be contributing directly to the change in cyclone developments.

The future change in zonal wind at 850 hPa shown in Fig. 7d is much smaller than that at 300 hPa (Fig. 7a), while the pattern of the change is similar around Europe and East Asia, occurring via vertical momentum transport from upper levels or via meridional heat transport by eddies. In the eddy kinetic energy at 850 hPa (Fig. 7e), the decreasing signals are stronger than the increasing signals, when compared with 300 hPa (Fig. 7b). The decreasing signal is especially pronounced in the area south of Japan, while the increasing signal is seen in the eastern Atlantic and near Alaska. A similar pattern is seen in the future change in meridional heat transport by eddies (not shown) and has been also seen in the future change in variability of SLP at a synoptic time scale obtained from the ensemble mean of the CMIP3 models themselves (Ulbrich et al. 2008). Figure 7f is the change in  $\sigma$  at 850 hPa. The values show a decrease over the middle-high latitudes, especially in the Pacific, and only a very small area shows an increase. This decrease is thought to be related to a decrease in the total number of cyclones (Geng and Sugi 2003; Yin 2005) and has a similar pattern to that also in our experiments (Fig. 4b). It is difficult to explain the increase in cyclone development (Fig. 5) in terms of these lower-level situations.

### c. Cyclone intensification and the upper troposphere

A correspondence is seen between regions of jet intensification in the upper troposphere (Fig. 7a) and regions

of intensified surface cyclone development (Fig. 5b) at a climatological time scale. To assess the correspondence at a monthly-mean time scale, scatter diagrams of upper-tropospheric zonal wind (average of 300–500 hPa) and cyclone growth rate for each month are shown in Fig. 8. Those for each month of DJF for 25 yr of the JRA-25, the three present-day experiments, and the three future experiments in the 60-km model averaged over the northwest Pacific ( $120^{\circ}\text{E}-180^{\circ}$ ,  $40^{\circ}-55^{\circ}\text{N}$ ; region P) and the North Atlantic ( $40^{\circ}\text{W}-0^{\circ}$ ,  $45^{\circ}-60^{\circ}\text{N}$ ; region A), where growth rate shows a marked increase (Fig. 5b), are plotted in Figs. 8a and 8b. In addition, those averaged over two regions ( $120^{\circ}\text{E}-180^{\circ}$ ,  $25^{\circ}-40^{\circ}\text{N}$ ; region P';  $40^{\circ}\text{W}-0^{\circ}$ ,  $30^{\circ}-45^{\circ}\text{N}$ ; region A'), where the growth rate decreases on the equatorial side of the region P and A, are also plotted in Figs. 8c and 8d.

Strong, positive correlations are seen in regions P and A in the JRA-25 reanalysis in the present-day experiments and in the future experiments (Figs. 8a,b), whereas weaker correlations are seen in regions P' and A' (Figs. 8c,d). Note that in region P, the growth rate shows a correlation with the meridional temperature gradient at lower levels ( $\sim 0.53$ ) but not as high as the upper-tropospheric zonal wind. Unlike the case of tropical cyclone development, neither humidity nor latent heat flux is correlated with cyclone growth rate (not shown), while tropical cyclones are likely to intensify in the future climate in response to an increase in water vapor via enhanced latent heat release (Oouchi et al. 2006; Bengtsson et al. 2007). In regions P and A, months

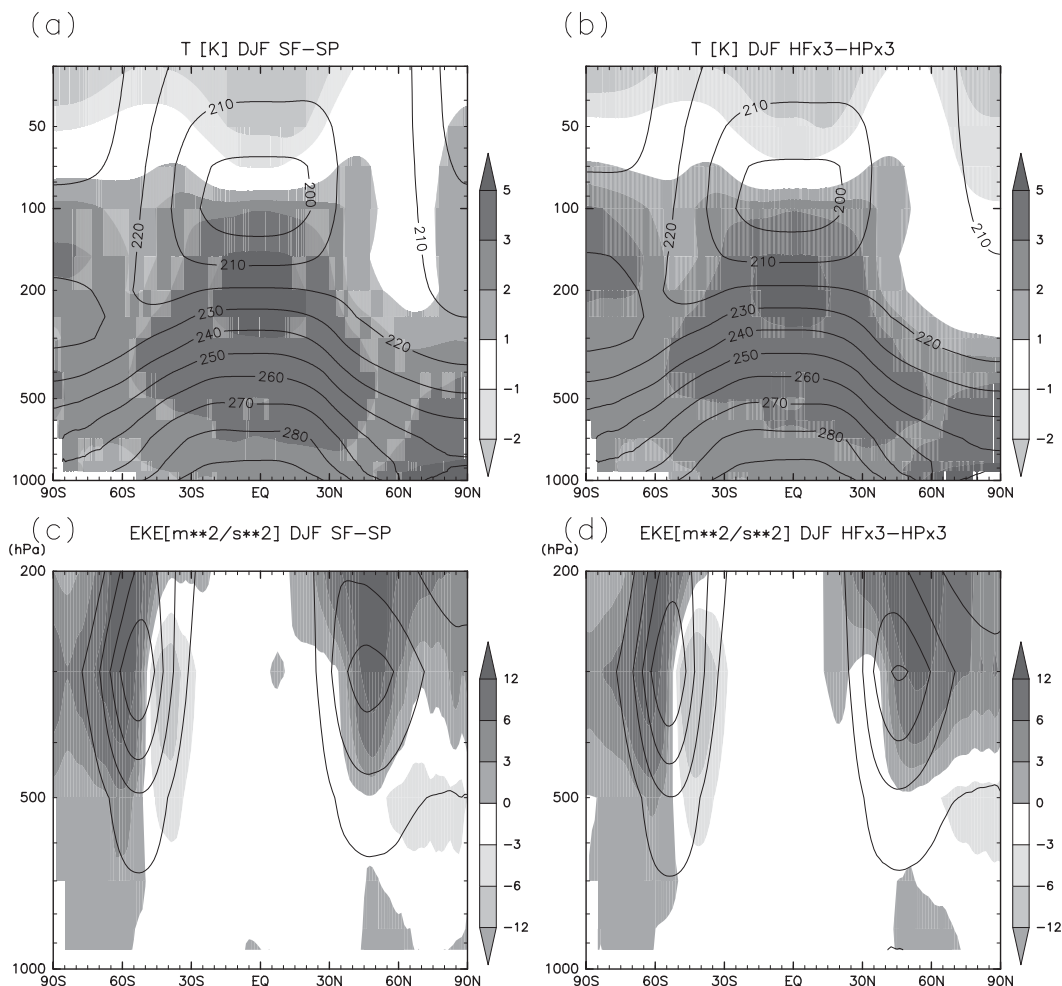


FIG. 6. Latitude–height sections of (a),(b) zonal mean temperature in units of K and (c),(d) zonal mean eddy kinetic energy at a synoptic time scale (2.5–8.0 days) in units of  $\text{m}^2 \text{s}^{-2}$  for (a),(c) the 20-km model and (b),(d) the three-member mean of the 60-km model. The contours show values of the present-day experiments (contour interval is  $40 \text{ m}^2 \text{ s}^{-2}$ ); shading indicates the difference between the present-day and future experiments.

with weak zonal wind ( $5\text{--}10 \text{ m s}^{-1}$ ) become less frequent in the future climate, and months with strong zonal wind ( $25\text{--}30 \text{ m s}^{-1}$ ) become more frequent. Consequently, months of high cyclone growth rate become more frequent, and months of low cyclone growth rate become less frequent.

To know what process could relate the upper-tropospheric wind speed to the surface cyclone growth rate in the region P and A, time evolutions in a shorter time scale are shown here for two extreme cases. Figure 9a shows a latitude–time cross section of 300-hPa zonal wind averaged over  $120^\circ\text{E}\text{--}180^\circ$  during the winter of 2090/91 of a member of the future experiments, when the January-mean growth rate in the region P is the highest among the months of January in the present-day and future experiments. Closed and open circles denote the latitudes and times of rapid surface cyclone development

in excess of  $30$  and  $25 \text{ hPa day}^{-1}$ , respectively. Most of the rapid developments are confined to  $35^\circ\text{--}55^\circ\text{N}$ . The rapid developments commonly correspond to the enhancements of the wind at these latitudes at a time scale of several days. At the same time, the jet is weakened around the core latitudes ( $30^\circ\text{--}40^\circ\text{N}$ ). Figure 9c shows 300-hPa zonal wind and rapid surface cyclone development during the winter of 1996/97 of a member of the present-day experiments, when the January-mean growth rate in the region P is the lowest. The zonal wind is steady throughout winter and is stronger (weaker) at lower (higher) latitudes. The rapid cyclone developments are sparse and limited to periods of minor displacement of the jet at around 3 and 15 January.

Snapshots of the Ertel's potential vorticity (PV) and wind vector at 300 hPa for a typical day during the January of Fig. 9a and one during the January of Fig. 9c

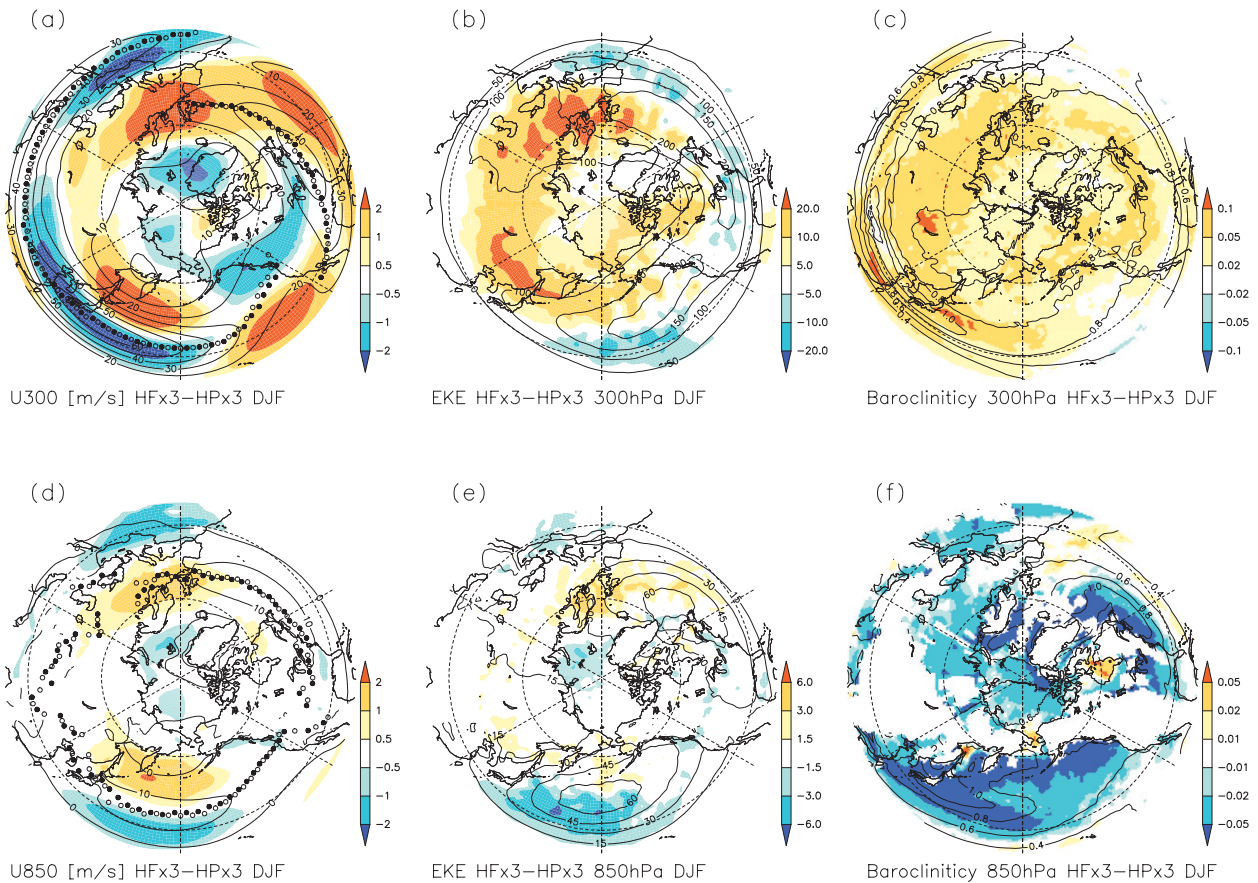


FIG. 7. Horizontal distributions of (a),(d) zonal wind in units of  $\text{m s}^{-1}$  and (b),(e) eddy kinetic energy at a synoptic time scale (2.5–8.0 days) in units of  $\text{m}^2 \text{s}^{-2}$  and (c),(f) the maximum Eady growth rate in units of  $\text{day}^{-1}$ , at (a)–(c) 300 hPa and (d)–(f) 850 hPa. The contours show values of the present-day experiments; shading indicates the difference between the present-day and future experiments. Open and closed circles in (a),(d) indicate the locations of maximum wind for each longitude for the present-day and future experiments, respectively.

are shown in Figs. 9b and 9d. On the month with the highest growth rate, anticyclonic wave-breaking patterns like Fig. 9b are frequently seen. This reflects anticyclonic shear is frequently dominant around the breaking region ( $40^{\circ}$ – $50^{\circ}\text{N}$ ). The jet is often fluctuated and displaced poleward, associated with the enhanced polar jet and the future increase in eddy kinetic energy in the upper troposphere (Fig. 7b). Closed and open circles denote the positions of rapid surface cyclone development in excess of 30 and 25  $\text{hPa day}^{-1}$ , respectively, between 0000 UTC of the previous day and 1800 UTC of that day. The rapid development of surface cyclones is seen near regions with strong southwesterly wind (Fig. 9b), where a strong horizontal PV gradient exists as a result of the displacement of high-PV air. In this case, the breaking pattern is found in the upstream of the rapid development. On the month with the lowest growth rate, the wave-breaking pattern is cyclonic like Fig. 9d throughout most of the month, reflecting the cyclonic shear around the region. This is associated with

the strong subtropical jet and a reduced frequency of meandering of the jet.

To assess the difference in the wave-breaking pattern in the upper troposphere between the months with the high growth rate and those with low growth rate, the wave-breaking pattern is categorized into LC1 type (anticyclonic shear) and LC2 type (cyclonic shear) and their frequencies are examined. One of the various categorizing methods proposed by Gabriel and Peters (2008) is used. If PV at a grid point satisfies  $\partial\text{PV}/\partial y < 0$  and  $\partial\text{PV}/\partial x > 0$ , the point is classified as LC1. If PV at a grid point satisfies  $\partial\text{PV}/\partial y < 0$  and  $\partial\text{PV}/\partial x < 0$ , the point is classified as LC2.

Three months with the highest growth rate in the region P are picked up for each of the three future experiments (a total of nine months, referred to as HG) and three months with the lowest growth rate in the region P are picked up for each of the three present experiments (a total of nine months, referred to as LG). Figure 10 compares the frequency of LC1 and LC2 at 300 hPa, for the

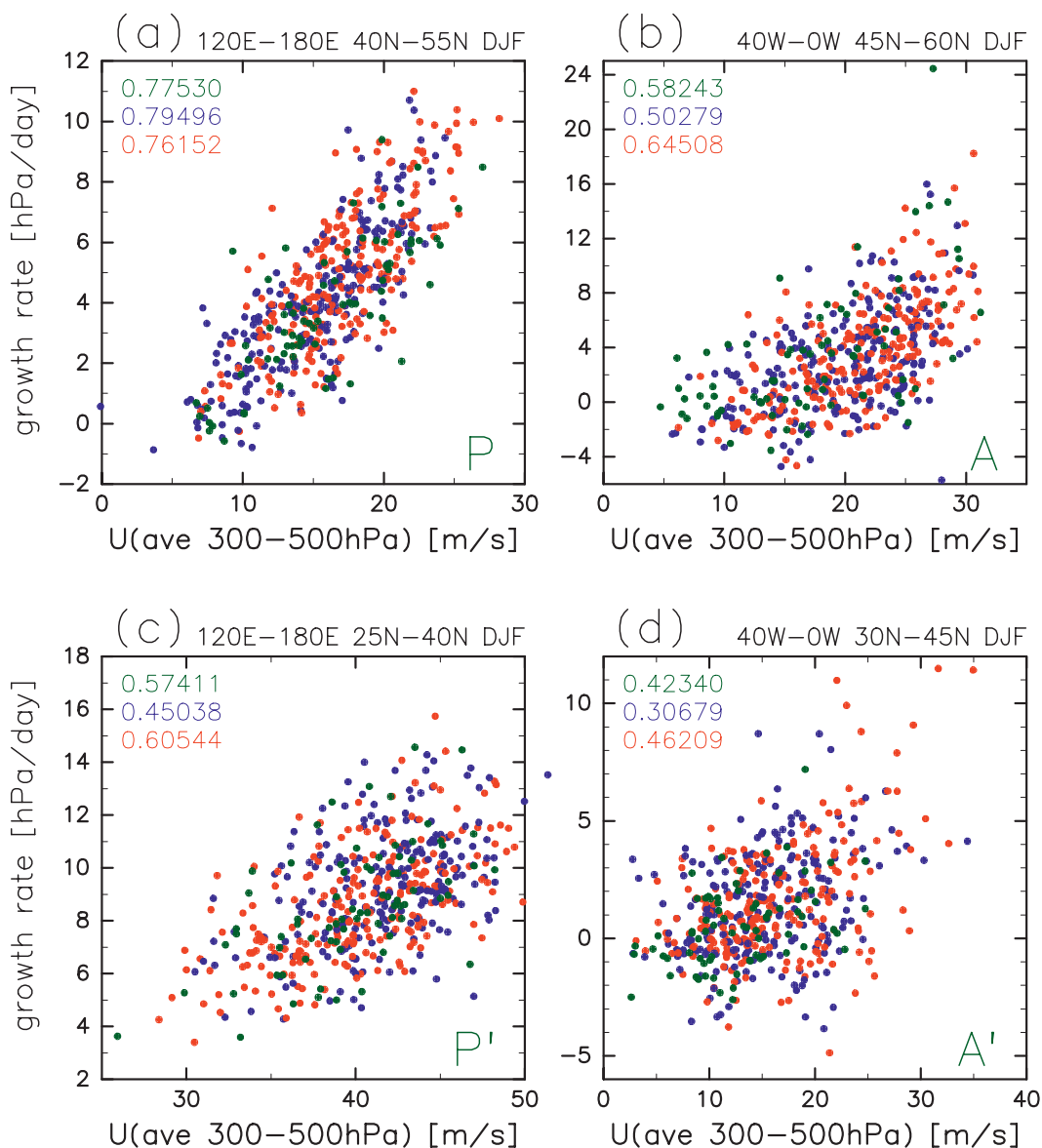


FIG. 8. Scatter diagrams of upper-tropospheric zonal wind averaged from 300 to 500 hPa and surface cyclone growth rate for each month, for the regions of (a) the northwest Pacific (120°E–180°, 40°–55°N; region P) and (b) the North Atlantic (40°W–0°, 45°–60°N; region A), (c) the equatorial side of region P (120°E–180°, 25°–40°N; region P') and (d) the equatorial side of region A (40°W–0°, 30°–45°N; region A'). Green, blue, and red points indicate JRA-25, the present-day experiments, and the future experiments, respectively, with their correlation coefficients.

average over HG and over LG. Because the height of the isentropic surface shows a marked change with global warming, the change is shown on the pressure surface.

In LG, occurrence of LC2 is more frequent (Fig. 10d) than that of LC1 (Fig. 10c) in most of the region P. Meanwhile, occurrence of LC1 (Fig. 10a) and LC2 (Fig. 10b) is more comparable in HG. Compared with LG, occurrence of LC1 in HG is more frequent over the western half of the region P (Fig. 10e), and occurrence of LC2 in HG is much less frequent not only within the

region P but also in its upstream and downstream. Note that comparing months with the highest and lowest growth rate within the three present experiments also gives similar results, with less pronounced difference (not shown).

Figure 11 is the result of the same calculation as Fig. 10 but for region A. A similar result to Fig. 10 is obtained also in region A. Occurrence of LC2 in HG is much less frequent than in LG not only within the region A but also in its upstream and downstream. Although occurrence

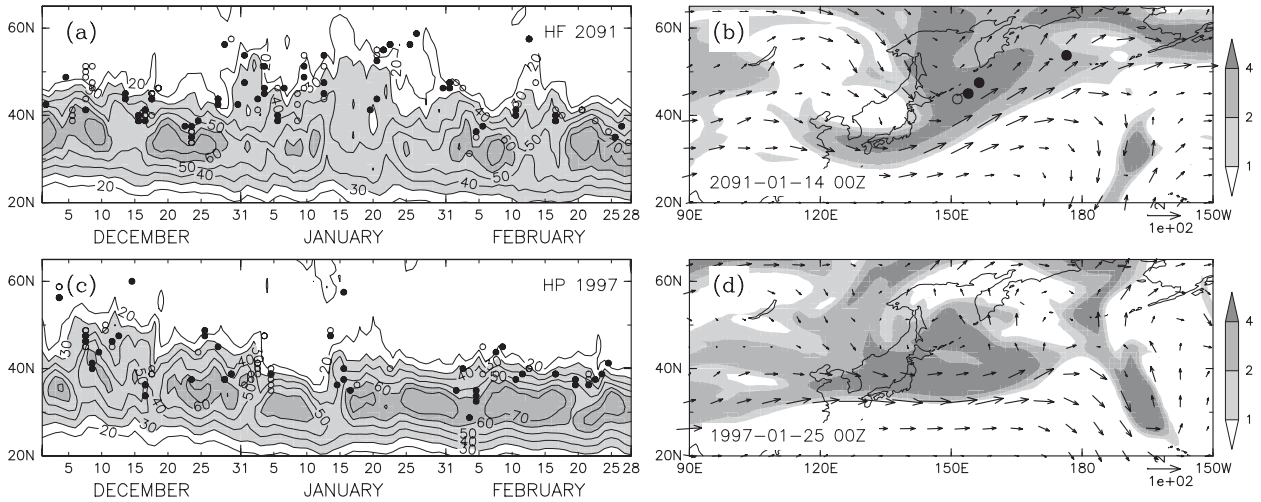


FIG. 9. (a),(c) Latitude–time cross section of 300-hPa zonal wind averaged over 120°E–180° from the previous DJF of (a) 2091 of a member of the future experiments, and (c) 1997 of a member of the present-day experiments. Closed and open circles denote the latitudes and times of rapid surface cyclone development in 120°E–180° in excess of 30 and 25 hPa day<sup>-1</sup>, respectively. (b),(d) Snapshots of the Ertel’s potential vorticity at 300 hPa (shading) and horizontal wind at 300 hPa (arrows) for (b) a typical day during (a), and for (d) a typical day during (c). The units of potential vorticity are PVU (1 PVU = 10<sup>-6</sup> K m<sup>2</sup> s<sup>-1</sup> kg<sup>-1</sup>). Closed and open circles denote the positions of rapid surface cyclone development in excess of 30 and 25 hPa day<sup>-1</sup>, respectively, between 0000 UTC of the previous day and 1800 UTC of the present day.

of LC1 does not show a marked difference within the region A, it is more frequent in the upstream, equatorial side around 60°–20°W, 20°–45°N. Under idealized simulations, averaged cyclone developments are more rapid under anticyclonic wave breakings, and lifetimes of the

cyclones become longer under cyclonic wave breakings (Thorncroft et al. 1993; Watanabe 2009). Although the relationships have not been statistically presented in the real atmosphere, the increase in occurrence of LC1 is consistent with the enhancement of cyclone development

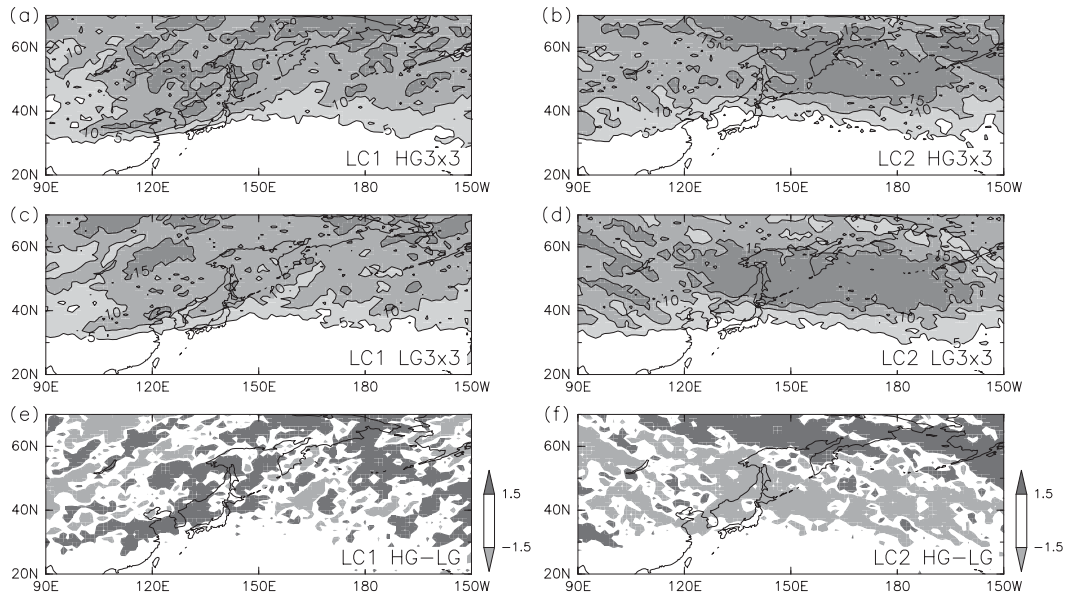


FIG. 10. Frequency distributions of (a),(c),(e) LC1-type and (b),(d),(f) LC2-type breakings at 300 hPa, in (a),(b) averaged over nine months with high growth rate in the region P, in (c),(d) averaged over nine months with low growth rate in the region P, and in (e),(f) the difference between the two. See text for details. The frequencies are calculated for each 2.5° grid box. Units are 1 per month per box.

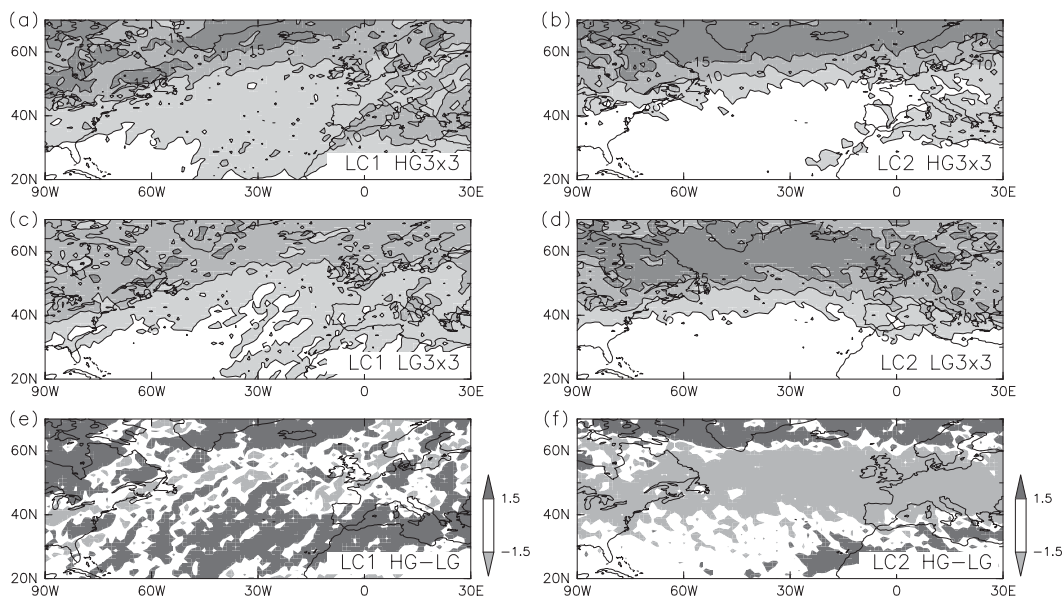


FIG. 11. As in Fig. 10, but for the region A.

in our model. Moreover, the decrease in occurrence of LC2 is also consistent with the decrease in long-lived cyclones (Fig. 3), especially for weak cyclones. Note that the regions of increase in occurrence of LC1 are not the same as regions P and A themselves. These shifts could exist because the wave breaking and rapid cyclone development are occurring at different locations.

Therefore, one of the possibilities that can explain the increasing growth rate in the future experiments is changes in wave-breaking pattern, that is, a decrease in wave breakings in areas of cyclonic shear and an increase in wave breakings in areas of anticyclonic shear. Associated with these changes, rapid cyclone developments can be more commonly seen, and weak, long-lived cyclones become less frequent.

#### 4. Summary and discussion

Future changes in wintertime cyclone behavior were investigated using a high-resolution AGCM forced by the SST change estimated by the CMIP3 multimodel ensemble mean. The total number of cyclones shows a decrease in future experiments. It is associated with a decrease in baroclinicity near the surface, resulting from a large temperature increase in the polar region. In contrast, the number of intense cyclones shows a future increase. The increase is seen on the polar side, downstream of the storm track. The increase in the synoptic-scale activity can be explained by the increase in intense cyclones in spite of the decrease in total cyclone number of cyclones. Cyclone development is enhanced in the areas upstream of regions with intense cyclones.

The regions with enhanced cyclone development correspond to regions with increasing zonal wind in the upper troposphere. In these regions, a strong correlation is seen between the upper-tropospheric zonal wind speed and the average surface cyclone growth rate at a monthly time scale. Months of high cyclone growth rate with strong zonal wind in these regions become more frequent, and months of low cyclone growth rate with weak zonal wind become less frequent. As a consequence of an enhanced upper-tropospheric polar jet, wave breaking in areas of cyclonic shear (LC2) is reduced and that in areas of anticyclonic shear (LC1) is increased. This could explain the enhancement of the surface cyclone developments. However, more studies are needed on the relationships between the breaking pattern and the cyclone development, which have not been statistically presented in the realistic atmosphere.

The zonal mean of zonal wind change (Figs. 7a,d) shows a decrease around 30°N and an increase around 50°N. This has an equivalent barotropic structure, associated with a positive change in the Arctic Oscillation index (Shindell et al. 1999; Yukimoto and Kodera 2005). Around the middle–upper troposphere at midlatitudes, an increase in the meridional temperature gradient leads to an increase in eddy kinetic energy at a synoptic time scale (Fig. 7b), and an increase in equatorward Eliassen–Palm (EP) flux, or poleward momentum flux, as a result of changes in the refractive index. These changes correspond to weakening of the jet at around 30°N and enhancement at around 50°N (Rind et al. 2005).

In contrast, the location of the baroclinic zone near the surface, where energy is supplied to the upper-tropospheric

Rosby wave, is influenced mainly by the meridional gradient of SST. In our experimental setting, the change in location of the strong SST gradient is not large. Therefore, the relative positions of the baroclinic zone and the jet are changed. Because the breaking pattern is determined largely by the relative position of the lower-tropospheric baroclinic zone and the upper-tropospheric jet (Thorncroft et al. 1993), wave breaking in areas of cyclonic shear (LC2) shows a decrease and that in areas of anticyclonic shear (LC1) shows an increase in the regions shown in Fig. 8.

Especially in the Pacific, development is suppressed in midwinter, known as the midwinter suppression (Nakamura 1992). Nakamura and Sampe (2002) showed that the suppression is due to the separation of the baroclinic zone and the subtropical jet. The reduced size of the separation in the future may affect the change in cyclone development via more frequent couplings (Inatsu and Kimoto 2005). Note that the small change in the location of the strong SST gradient may reflect the experimental setup, in which the change in SST gradient in the CMIP3 models is smoothed by taking the ensemble mean.

Much of the change at lower altitudes tends to result in weaker cyclone activity (Fig. 7e), except for changes in wind and water vapor. The future change in wind at lower levels (Fig. 7d) is derived mainly from the upper level (Fig. 7a) via vertical momentum transport by baroclinic eddies. The change in water vapor can result in enhanced cyclone development. In fact, tropical cyclones are likely to intensify in the future climate experiments, although the number of storms is likely to be reduced; their intensification is related to an increase in water vapor (Oouchi et al. 2006; Bengtsson et al. 2007). Although latent heat flux from the surface shows an increase also in the winter extratropics, the correlation between the flux and the cyclone growth rate is weaker than that between the flux and the jet. Furthermore, the increase in the latent heat flux cannot explain the decrease in cyclone growth at around 30°N (Fig. 5b), indicating that it is not a crucial factor, although it may play supplementary role on the change in cyclone development.

Because higher-resolution models have an advantage in representing the locations of storm tracks and blockings, especially in the Atlantic (Matsueda et al. 2009), such models are suitable for investigating future changes in storm behavior. In the same experiments as those analyzed in the present study, Matsueda et al. (2009) showed the frequency of blocking events are reduced in the future experiments, especially on the western side of the present peaks. Moreover, using long-term ensemble simulations are needed to obtain more statistically significant change because phenomena in the wintertime extratropics have large internal, interannual variability. The detection of

such changes from observational data is currently a difficult task. Using long-term and high-resolution simulations, it would be possible to examine, as a topic for a future study, the nature of the relationships between the change in cyclones shown in the present study and other changes such as blockings, heat transport by transient or stationary waves, and the Arctic Oscillation. However, even in the case that SST change is given by the ensemble mean of the CMIP3 models, the present results are from a single atmospheric model. Once long-term, high-resolution simulations have been performed using many other models, many more things would be clarified through a comparison of the simulation results.

*Acknowledgments.* This work was supported by the “Projection of the Change in Future Weather Extremes using Super-High-Resolution Atmospheric Models” project as part of the KAKUSHIN Program by the Ministry of Education, Culture, Sports, Science and Technology of Japan. The model calculations were made on the Earth Simulator. The GFD-DENNOU Library was used for making the figures. We thank two anonymous reviewers for constructive comments.

#### REFERENCES

- Bengtsson, L., K. I. Hodges, and E. Roeckner, 2006: Storm tracks and climate change. *J. Climate*, **19**, 3518–3543.
- , —, M. Esch, N. Keenlyside, L. Kornblueh, J.-J. Luo, and T. Yamagata, 2007: How May tropical cyclones change in a warmer climate? *Tellus*, **59A**, 539–561.
- , —, and N. Keenlyside, 2009: Will extratropical storms intensify in a warmer climate? *J. Climate*, **22**, 2276–2301.
- Gabriel, A., and D. Peters, 2008: A diagnostic study of different types of Rossby wave breaking events in the Northern extratropics. *J. Meteor. Soc. Japan*, **86**, 613–631.
- Geng, Q. Z., and M. Sugi, 2003: Possible change of extratropical cyclone activity due to enhanced greenhouse gases and sulfate aerosols—Study with a high-resolution AGCM. *J. Climate*, **16**, 2262–2274.
- Hall, A., 2004: The role of surface albedo feedback in climate. *J. Climate*, **17**, 1550–1568.
- Inatsu, M., and M. Kimoto, 2005: Two types of interannual variability of the mid-winter storm tracks and their relationship to global warming. *SOLA*, **1**, 61–64.
- Jung, T., S. K. Gulev, I. Rudeva, and V. Soloviev, 2006: Sensitivity of extratropical cyclone characteristics to horizontal resolution in the ECMWF model. *Quart. J. Roy. Meteor. Soc.*, **132**, 1839–1857.
- Kitoh, A., and Coauthors, 2009: Projection of changes in future weather extremes using super-high-resolution global and regional atmospheric models in the KAKUSHIN Program: Results of preliminary experiments. *Hydro. Res. Lett.*, **3**, 49–53.
- Lambert, S. J., and J. C. Fyfe, 2006: Changes in winter cyclone frequencies and strengths simulated in enhanced greenhouse warming experiments: Results from the models participating in the IPCC diagnostic exercise. *Climate Dyn.*, **26**, 713–728.

- Lindzen, R. S., and B. F. Farrell, 1980: A simple approximate result for maximum growth rate of baroclinic instabilities. *J. Atmos. Sci.*, **37**, 1648–1654.
- Matsueda, M., R. Mizuta, and S. Kusunoki, 2009: Future change in wintertime atmospheric blocking simulated using a 20-km-mesh atmospheric global circulation model. *J. Geophys. Res.*, **114**, D12114, doi:10.1029/2009JD011919.
- Meehl, G., C. Covey, T. Delworth, M. Latif, B. McAvaney, J. Mitchell, R. Stouffer, and K. Taylor, 2007: The WCRP CMIP3 multimodel dataset: A new era in climate change research. *Bull. Amer. Meteor. Soc.*, **88**, 1383–1394.
- Mizuta, R., and Coauthors, 2006: 20-km-mesh global climate simulations using JMA-GSM model: Mean climate states. *J. Meteor. Soc. Japan*, **84**, 165–185.
- , Y. Adachi, S. Yukimoto, and K. Kusunoki, 2008: Estimation of future distribution of sea surface temperature and sea ice using CMIP3 multi-model ensemble mean. Meteorological Research Institute Tech. Rep. 56, 28 pp.
- Nakamura, H., 1992: Midwinter suppression of baroclinic wave activity in the Pacific. *J. Atmos. Sci.*, **49**, 1629–1641.
- , and T. Sampe, 2002: Trapping of synoptic-scale disturbances into the North-Pacific subtropical jet core in midwinter. *Geophys. Res. Lett.*, **29**, 1761, doi:10.1029/2002GL015535.
- Onogi, K., and Coauthors, 2007: The JRA-25 Reanalysis. *J. Meteor. Soc. Japan*, **85**, 369–432.
- Oouchi, K., J. Yoshimura, H. Yoshimura, R. Mizuta, S. Kusunoki, and A. Noda, 2006: Tropical cyclone climatology in a global-warming climate as simulated in a 20 km-mesh global atmospheric model: Frequency and wind intensity analyses. *J. Meteor. Soc. Japan*, **84**, 259–276.
- Pinto, J. G., U. Ulbrich, G. C. Leckebusch, T. Spanghel, M. Reyers, and S. Zacharias, 2007: Changes in storm track and cyclone activity in three SRES ensemble experiments with the ECHAM5/MPIOM1 GCM. *Climate Dyn.*, **29**, 195–210.
- Rayner, N. A., D. E. Parker, E. B. Horton, C. K. Folland, L. V. Alexander, D. P. Rowell, E. C. Kent, and A. Kaplan, 2003: Global analyses of sea surface temperature, sea ice, and night marine air temperature since the late nineteenth century. *J. Geophys. Res.*, **108**, 4407, doi:10.1029/2002JD002670.
- Rind, D., J. Perlwitz, and P. Lonergan, 2005: AO/NAO response to climate change: 1. Respective influences of stratospheric and tropospheric climate changes. *J. Geophys. Res.*, **110**, D12107, doi:10.1029/2004JD005103.
- Shapiro, M. A., and Coauthors, 1999: A planetary-scale to meso-scale perspective of the life cycles of extratropical cyclones: The bridge between theory and observations. *The Life Cycles of Extratropical Cyclones*, M. A. Shapiro and S. Grønås, Eds., Amer. Meteor. Soc., 139–185.
- Shindell, D., R. Miller, G. Schmidt, and L. Pandolfo, 1999: Simulation of recent northern winter climate trends by greenhouse-gas forcing. *Nature*, **399**, 452–455.
- Solomon, S., D. Qin, M. Manning, M. Marquis, K. Averyt, M. M. B. Tignor, H. L. Miller Jr., and Z. Chen, Eds., 2007: *Climate Change 2007: The Physical Science Basis*. Cambridge University Press, 996 pp.
- Thorncroft, C. D., B. J. Hoskins, and M. McIntyre, 1993: Two paradigms of baroclinic-wave life-cycle behavior. *Quart. J. Roy. Meteor. Soc.*, **119**, 17–55.
- Ulbrich, U., J. G. Pinto, H. Kupfer, G. C. Leckebusch, T. Spanghel, and M. Reyers, 2008: Changing Northern Hemisphere storm tracks in an ensemble of IPCC climate change simulations. *J. Climate*, **21**, 1669–1679.
- , G. C. Leckebusch, and J. G. Pinto, 2009: Extra-tropical cyclones in the present and future climate: A review. *Theor. Appl. Climatol.*, **96**, 117–131.
- Watanabe, M., 2009: Self-limiting feedback between baroclinic waves and a NAO-like sheared zonal flow. *Geophys. Res. Lett.*, **36**, L08803, doi:10.1029/2009GL037176.
- Wernli, H., R. Fehlmann, and D. Lüthi, 1998: The effect of barotropic shear on upper-level induced cyclogenesis: Semi-geostrophic and primitive equation numerical simulations. *J. Atmos. Sci.*, **55**, 2080–2094.
- Winton, M., 2006: Amplified Arctic climate change: What does surface albedo feedback have to do with it? *Geophys. Res. Lett.*, **33**, L03701, doi:10.1029/2005GL025244.
- Yin, J. H., 2005: A consistent poleward shift of the storm tracks in simulations of 21st century climate. *Geophys. Res. Lett.*, **32**, L18701, doi:10.1029/2005GL023684.
- Yoshiike, S., and R. Kawamura, 2009: Influence of wintertime large-scale circulation on the explosively developing cyclones over the western North Pacific and their downstream effects. *J. Geophys. Res.*, **114**, D13110, doi:10.1029/2009JD011820.
- Yukimoto, S., and K. Kodera, 2005: Interdecadal Arctic Oscillation in twentieth century climate simulations viewed as internal variability and response to external forcing. *Geophys. Res. Lett.*, **32**, L03707, doi:10.1029/2004GL021870.